



**Karolinska
Institutet**

Karolinska Institutet

<http://openarchive.ki.se>

This is a Peer Reviewed Accepted version of the following article, accepted for publication in EMBO Reports.

2016-12-07

High density of REC8 constrains sister chromatid axes and prevents illegitimate synaptonemal complex formation

Agostinho, Ana; Manneberg, Otto; van Schendel, Robin; Hernández-Hernández, Abrahan; Kouznetsova, Anna; Blom, Hans; Brismar, Hjalmar; Höög, Christer

EMBO Rep. 2016 Jun;17(6):901-13.

<http://doi.org/10.15252/embr.201642030>

<http://hdl.handle.net/10616/45426>

If not otherwise stated by the Publisher's Terms and conditions, the manuscript is deposited under the terms of the Creative Commons Attribution-NonCommercial-NoDerivatives License (<http://creativecommons.org/licenses/by-nc-nd/4.0/>), which permits non-commercial re-use, distribution, and reproduction in any medium, provided the original work is properly cited, and is not altered, transformed, or built upon in any way.

High density of REC8 constrains sister-chromatid axes and prevents illegitimate synaptonemal complex formation

Ana Agostinho^{1*}, Otto Manneberg², Robin van Schendel³, Abrahan Hernández-Hernández¹, Anna Kouznetsova¹, Hans Blom², Hjalmar Brismar² and Christer Höög¹

¹ Department of Cell and Molecular Biology, Karolinska Institutet, Berzelius väg 35, 171 77 Stockholm, Sweden

² Science for Life Laboratory, Dept of Applied Physics, Royal Institute of Technology, PO Box 1031, 17121, Solna, Sweden

³ Department of Human Genetics, Leiden University Medical Center, PO Box 9600, 2300 RC, Leiden, The Netherlands

*Corresponding Author

Ana Agostinho

Department of Cell and Molecular Biology

Karolinska Institutet

Berzelius väg 35

171 77 Stockholm, Sweden

Tel: +46852487386

Fax: +468323672

E-mail: ana.agostinho@ki.se

Number of characters: 42.479

Running title: High density of REC8 prevents inter-sister synapsis

1 **Abstract**

2

3 During meiosis, cohesin complexes mediate sister-chromatid cohesion (SCC), synaptonemal
4 complex (SC) assembly and synapsis. Here, using super-resolution microscopy, we image
5 sister-chromatid axes in mouse meiocytes that have normal or reduced levels of cohesin
6 complexes, assessing the relationship between localization of cohesin complexes, SCC and
7 SC formation. We show that REC8 foci are separated from each other by a distance smaller
8 than 15% of the total chromosome axis length in wild-type meiocytes. Reduced levels of
9 cohesin complexes result in a local separation of sister-chromatid axial elements (LSAE), as
10 well as illegitimate SC formation at these sites. REC8, but not RAD21 or RAD21L-cohesin
11 complexes flank sites of LSAE, whereas RAD21 and RAD21L appear predominantly along
12 the separated sister-chromatid axes. Based on these observations and a quantitative
13 distribution analysis of REC8 along sister-chromatid axes, we propose that the high density of
14 randomly distributed REC8 cohesin complexes promotes SCC and prevents illegitimate SC
15 formation.

16

17 **Keywords:** cohesin/ meiosis/ super-resolution microscopy/ synaptonemal complex/ sister-
18 chromatid cohesion

19

1 Introduction

2
3 Sister-chromatid cohesion (SCC) ensures that chromosomes are correctly segregated in
4 mitotic and meiotic cells [1]. SCC is established during DNA replication by cohesin complexes.
5 These multi-subunit protein complexes form ring-like structures that hold the newly replicated
6 sister-chromatids together from S-phase until anaphase.

7 During meiosis, cohesion along chromosome arms is lost prior to anaphase I to allow
8 the segregation of homologous chromosomes (homologs), whereas centromeric cohesion is
9 released prior to anaphase II to allow segregation of sister-chromatids. In vertebrates, the
10 mitotic cohesin complex is composed of four core components: two structural maintenance of
11 chromosomes (SMC) proteins, SMC1 α and SMC3, the α -kleisin RAD21 and one of two
12 stromal antigen (SA) proteins SA1 or SA2 (also called STAG1 and STAG2). Several meiosis
13 specific components have been identified in mammals, including: SMC1 β , α -kleisins REC8
14 and RAD21L and SA protein SA3/STAG3 [2-10].

15 Meiotic cohesin complexes contribute to the assembly of the synaptonemal complex
16 (SC), a meiosis-specific structure that facilitates crossover recombination by tethering two
17 homologs. The SC has a characteristic tripartite ladder-like structure; approximately 100 nm
18 wide [11,12], where transverse filaments connect a central element to the lateral elements
19 (LEs) (AEs are referred to as LEs upon synapsis) of each homolog. Several SC proteins have
20 been identified in mammals: AE proteins SYCP2 and SYCP3, transverse filament protein
21 SYCP1 and central element proteins SYCE1, SYCE2, SYCE3 and TEX12 [13-19].

22 AEs assemble along the axis of sister chromatids at the leptotene stage of meiosis I
23 [20], possibly as two separate parallel structures that are tightly associated [21]. Synapsis
24 (tethering two homologs) then commences at the zygotene stage of meiosis I, when the AEs
25 of the two homologs become progressively juxtaposed. SC formation is complete at the
26 pachytene stage of meiosis I, concomitant with the completion of reciprocal crossover events
27 (for review see [22]).

28 SMC1 β is first detected on sister chromatids at the leptotene stage of meiosis I, and
29 remains at centromeres of chromosomes until the anaphase stage of meiosis II [2,10,23].
30 *Smc1 β ^{-/-}* spermatocytes have been shown to have impaired SCC, incomplete synapsis and

1 to display shortened AEs with extensions of chromatin loops, suggesting a structural role for
2 SMC1 β in meiotic chromosome axis organization [23,24]. Premature loss of chromosome
3 arm and centromeric cohesion at the first meiotic division in *Smc1 β ^{-/-}* oocytes, leads to high
4 levels of chromosome missegregation, resulting in sterility [23].

5 Three different α -kleisins have been shown to be expressed in mammalian meiotic
6 cells. REC8 is detected on chromosomes prior to DNA replication at the pre-leptotene stage
7 of meiosis I and remains bound at centromeres until the anaphase stage of meiosis II. *Rec8^{-/-}*
8 mice retain SCC at the centromeres but exhibit loss of SCC along chromosome arms [25,26].
9 SC formation occurs illegitimately between sister-chromatids in *Rec8^{-/-}* mice [25,26],
10 suggesting an active role of REC8 in directing SC formation to take place between homologs,
11 and thus the existence of a cohesin-based regulatory mechanism for SC assembly and
12 synapsis.

13 RAD21L appears on chromosomes after DNA replication and declines after the
14 pachytene stage of meiosis I [4,5]. *Rad21L^{-/-}* spermatocytes retain SCC but display impaired
15 synapsis, where SCs form predominantly between non-homologous chromosomes [27,28].

16 RAD21 is detected at chromosomes at the pachytene stage of and remains bound to
17 centromeres at the metaphase stage of meiosis I. Contradictory results regarding the
18 expression of RAD21 prior to the pachytene stage of meiosis I have been reported
19 [4,5,8,29,30], and the absence of a meiotic mutant with selective abrogation of RAD21 has
20 prevented a direct study of the contribution of this α -kleisin to meiotic SCC. Based on the
21 studies of *Rec8^{-/-}* mice, however, it has been proposed that REC8, and not RAD21, is
22 responsible for the canonical cohesion function (i.e., holding sister-chromatids together) in
23 meiotic cells [4,5,28].

24 Finally, STAG3 is detected uniformly on chromosomes from the leptotene stage to
25 the diplotene stage of meiosis I. STAG3 is required for stabilization of REC8 cohesin
26 complexes and their association with the meiotic chromosome axes [31-33]. Accordingly,
27 hypomorphic *Stag3* mutant mice with a severe loss of STAG3 expression display a limited
28 amount of REC8 and a phenotype similar to that of *Rec8^{-/-}* mice, including impaired meiotic
29 recombination and aberrant SC formation, predominantly between the shortened AEs of
30 sister-chromatids [31].

1 Here, we have employed super-resolution microscopy to study the role of different
2 mammalian meiotic cohesin-core components in SCC establishment/maintenance and SC
3 formation. We detected local separation of sister-chromatid axial elements (LSAE) in
4 univalent chromosomes of hypomorphic *Stag3* mutant and *Smc1 β ^{-/-}* spermatocytes,
5 accompanied by illegitimate SC formation at these sites. Sites of LSAE were flanked by REC8,
6 but not, RAD21 or RAD21L cohesin complexes. We propose, based on a quantitative
7 distribution analysis of REC8 foci along sister-chromatid axes, that local separation of sister-
8 chromatid AEs is prevented by a high density of randomly distributed, yet closely juxtaposed,
9 REC8-containing cohesin complexes.
10

Results

Separation of sister-chromatid axes revealed by super-resolution microscopy

In cells at the pachytene stage of meiosis I, a distance of approximately 100 nm separates paired AEs. This distance is smaller than the diffraction limit of conventional light microscopes (approximately 250 nm), therefore, in order to study axis organization in genetic backgrounds with different levels of REC8-mediated cohesion, nuclear spreads were analysed with super-resolution Structured Illumination Microscopy (SIM). Wild-type, *Rec8*^{-/-} and homozygous *Stag3*^{TgTn(sb□cHS4, Tyr)2312Cove} (a hypomorphic allele referred hereafter as *Stag3* mutant [31]) mutant spermatocytes were immunostained with antibodies against AE protein SYCP3, and an anti-centromere antibody (ACA). In wild-type pachytene cells, the two sister-chromatids of each homolog are tightly associated and were here detected in a single AE (Fig 1A), whereas the AEs of synapsed homologs (bivalents) were detected as two parallel SYCP3-labeled structures with associated telocentric centromeres (Fig 1A). In *Rec8*^{-/-} spermatocytes, where the sister-chromatids of univalents have lost their tight association provided by REC8-mediated cohesion, two separate AEs are observed [25,26]. Univalents could thus be visualized in *Rec8*^{-/-} spermatocytes harboring two discernible SYCP3-labeled sister-chromatid AEs (referred hereafter for simplification, as sister-AEs) with associated centromeres (Fig 1A).

REC8 levels are strongly reduced in *Stag3* mutant mice [31]. Consistently, and similarly to *Rec8*^{-/-} spermatocytes, SYCP3-labeled axes detected in *Stag3* mutant spermatocytes at a zygotene-like stage, displayed two separated sister-AEs (Fig 1B, magnified view). Consistent with a reduction, but not an abrogation of REC8 expression, sister-chromatids closely associated in a single AE could also be detected (Fig 1B, magnified view). We found that 69% of axes (288/414 axes associated with centromeres, from 11 nuclei) in *Stag3* mutant spermatocytes displayed some degree of sister-AE separation, whereas the remaining 31% of sister-chromatids appeared length-wise conjoined in a single AE (126/414 axes, Fig 1B, graph). Sister-chromatids displaying AE separation were subsequently grouped into two classes: those that displayed extensive separation (as shown

in Fig 1B, centre) and those that displayed restricted sites with local separation of AEs (LSAE) along the axes or close to the centromeres (Fig 1C). LSAE was detected in 34% of axes (142/414 axes) whereas extensive separation of AEs was detected on 35% of axes (146/414 axes) (Fig 1C, graph). Despite the occurrence of LSAE close to the centromeres, these were not separated, as shown by the close association of the two ACA foci (Fig 1C).

Given the presence of univalents in *Smc1 β ^{-/-}* spermatocytes [23,24], we next investigated the occurrence of LSAEs in this mutant background (Fig 1D). 16% of all univalent axes (65/404 axes, from 10 nuclei) displayed sites of LSAE, whereas extensive separation of AEs was never observed (Fig 1D, graph) in this mutant. The presence of LSAE in *Stag3* mutant and *Smc1 β ^{-/-}* spermatocytes was separately confirmed using Stimulated Emission Depletion (STED) microscopy (Fig 1E). The chromosomal regions at which LSAE was observed in *Stag3* mutant and *Smc1 β ^{-/-}* spermatocytes, were further characterized by comparing the inter axis-distances measured at these sites with the inter-axis distances between the AEs of synapsed wild-type homologs and the inter-axis distances between the sister-AEs of *Rec8^{-/-}* univalents (Fig 1F and Fig 1H). The median inter-axis distance at sites of LSAE in both *Stag3* mutant and *Smc1 β ^{-/-}* spermatocytes (150-175 nm), was similar to that of AEs of synapsed wild-type homologs and sister-AEs of *Rec8^{-/-}* univalents (Fig 1F). No difference in inter-axis distance between at sites of LSAE was detected in *Stag3* mutant univalents, irrespectively of where LSAEs were localized along the axis of chromosomes (Fig 1G).

In summary, we found that changes in the levels of STAG3, SMC1 β and REC8, to a variable degree contribute to local and extensive separation of sister-AEs.

Illegitimate synapsis takes place at sites of local separation of AEs

Illegitimate SC assembly occurs between the sister-AEs in *Rec8^{-/-}* spermatocytes [25,26]. In this mutant background, upon synapsis, AE/LEs have been shown to be separated by a distance similar to that of wild-type AE/LEs of synapsed homologs [26]. Since the inter-axis distances measured at the sites of LSAE in *Stag3* mutant and *Smc1 β ^{-/-}* spermatocytes were comparable to the distances separating the AEs of wild-type and *Rec8^{-/-}* spermatocytes (Fig

1 1F), we analysed whether inter-sister SC formation took place at sites of LSAE in *Stag3*
2 mutant and *Smc1 β ^{-/-}* spermatocytes. Transverse filament protein SYCP1 was detected within
3 the sites of LSAEs in *Stag3* mutant and *Smc1 β ^{-/-}* spermatocytes, as well as between the AEs
4 of wild-type chromosomes and the sister-AEs of *Rec8^{-/-}* univalents (Fig 2A, filled arrowhead
5 and Fig EV1 A). 95% of *Stag3* sister-chromatids with LSAE (114/120 affected axes) and 78%
6 of *Smc1 β ^{-/-}* sister-chromatids (53/68 affected axes) assembled SCs at these regions (Fig 2A,
7 graphs). Additional SC components such as SYCE1, SYCE2 and TEX12 were also detected
8 within sites of LSAE, in *Stag3* mutant and *Smc1 β ^{-/-}* spermatocytes (Fig 2B, filled arrowheads
9 and Fig EV1 B).

10 Quantification of signal distribution within the regions of LSAE in *Stag3* mutant
11 spermatocytes further demonstrated the formation of a tripartite SC: two SYCP3 intensity
12 peaks (Fig 2C, empty arrowheads) flanked one peak of TEX12, SYCE2, SYCE1 or TEX12.
13 We note that the C-terminal region of SYCP1 is located within the AEs, explaining the
14 appearance of two small peaks within the SYCP3 signal for this protein (Fig 2C, filled
15 arrowheads). These results show that tripartite SC formation occurs at sites of LSAE in *Stag3*
16 mutant and *Smc1 β ^{-/-}* spermatocytes.

18 **Sites with local separation of AEs are flanked by the REC8-cohesin subunit**

19
20 We next accessed the distribution of the individual α -kleisins (REC8, RAD21L and RAD21) in
21 relation to LSAE. *Stag3* mutant and *Smc1 β ^{-/-}* spermatocytes were immunostained with
22 antibodies against SYCP3, SYCE1 and one of the three α -kleisins: REC8, RAD21L and
23 RAD21. REC8 was detected co-localizing with SYCP3-labeled AEs of wild-type
24 chromosomes throughout meiotic prophase (Fig EV2 A). RAD21L starts to disappear from the
25 chromosome axes during the pachytene stage in wild-type spermatocytes, being only weakly
26 detectable by the diplotene stage (Fig EV2 B). Coinciding with the gradual disappearance of
27 RAD21L, RAD21 was detected from the pachytene to the diplotene stages of meiosis I in
28 wild-type spermatocytes (Fig EV2 C). We found that in *Stag3* mutant, as well as in *Smc1 β ^{-/-}*
29 spermatocytes, REC8 foci were detected flanking the sites of LSAE (Fig 3A, and Fig EV3 A).
30 A vast majority (81%) of LSAE sites in *Stag3* mutant axes (63/78 axes analysed in 13 nuclei)

1 had closely flanking REC8 foci (Fig 3A, graph and Fig 3D). RAD21L and RAD21 were
2 frequently found overlapping with sister-AEs in *Stag3* mutant and *Smc1 β ^{-/-}* spermatocytes,
3 but not flanking regions of LSAE (Fig 3B, C, D and Fig EV3 B and C), implying that local
4 presence of RAD21L does not restrict LSAE.

5 In agreement with these results, the expression of RAD21L and RAD21 in *Rec8^{-/-}*
6 spermatocytes was not sufficient to prevent extensive separation of AEs (Fig 3B and Fig EV3
7 D, E [28]). Thus, while all three different α -kleisins associate with the axes, the localization of
8 REC8 flanking LSAE, strongly suggests that only REC8 directly prevents LSAEs during
9 meiosis.

11 **A high density of REC8 prevents LSAEs and illegitimate SC assembly in wild-type** 12 **spermatocytes**

14 The X and Y sex chromosomes share only a short homology region called the pseudo
15 autosomal region (PAR) (Fig 4A, filled arrowhead) [34,35]. PAR undergoes crossover
16 recombination and synapsis during meiosis, whereas the rest of X and Y-chromosomes
17 remain unsynapsed and in this sense have an organization similar to what is observed in
18 univalent chromosomes. We used this feature of sex chromosomes to analyse the distribution
19 of REC8 along the axes of unsynapsed sister-chromatids in wild-type spermatocytes. We first
20 measured the inter-axis distances along sister-AEs of X-chromosomes, in wild-type
21 spermatocytes (Fig 4B, scheme). We found the AEs to be separated by a median distance of
22 100 nm, a significantly narrower inter-axis distance than observed at sites of LSAEs in the
23 *Stag3* mutant (Fig 4B, graph). In order to identify regions along X-chromosomes at which SC
24 formation is observed, wild-type pachytene spermatocytes were immunostained with
25 antibodies against SYCP3 and SYCE2. SYCE2 was detected abundantly at the PAR but only
26 sporadically between sister-AEs of the X-chromosomes (Fig 4C). Importantly, while short
27 regions of AE separation were observed along the X-chromosomes, SYCE2 was absent from
28 these regions (Fig 4C, empty arrowhead).

29 To analyse the distribution of REC8 along sister-AEs of X-chromosomes, individual
30 X-chromosomes were computationally straightened and divided into 25 regular intervals. We

1 detected an average of 16 REC8 foci per X-chromosome (n=225, for 14 X-chromosomes
2 analysed) (Fig 5A). The distribution of REC8 foci between the 25 intervals did not deviate
3 substantially from the average that reflects an evenly spread foci distribution (dotted line), with
4 the exceptions of the PAR and the terminal region of the X-chromosomes (corresponding to
5 the centromeric domain), at which a higher density of REC8 was observed (Fig 5B). Thus,
6 REC8 foci appear randomly distributed along AEs, excluding the terminal regions. We also
7 analysed the frequency distribution of inter-REC8 distances along the sister-AEs of X-
8 chromosomes. We found the majority of REC8 foci (95%) to be separated by a relative short
9 distance: less than ~15% of the chromosome axis length (Fig 5C, grey area in histogram).

10 The typical small distances between adjacent REC8 foci could result from an active
11 mechanism, such as genetic interference which ensures an even spacing of recombination
12 events along the axis of chromosomes [36], or be due to a random distribution of a high
13 number of REC8 foci per chromosome. To distinguish between these two possibilities, we first
14 estimated the strength of interference among REC8 foci by fitting the frequency distribution of
15 inter-focus distances to the gamma distribution. The result is a best-fit probability density
16 curve of which the shape parameter (ν) is a relative indicator of interference strength (the
17 higher the value of ν , the stronger the interference and the more evenly distributed the foci
18 are [36]). The theoretical interference level of randomly distributed foci is equal to 1,
19 nevertheless inter-focus distances smaller than 1.4% of the chromosomes length can not be
20 detected due to the resolution limit of our method. Thus, we simulated random foci
21 distributions using this value as a constraint (see methods section for details), and compared
22 the level of interference obtained for randomly simulated foci distributions (ν') with that
23 obtained for the experimental inter-REC8 distances (ν). The low level of interference detected
24 ($\nu=2.9$) (Fig 5D) and the similarity between $\nu=2.9$ (s.e. 0.27) and $\nu'=2.4$ (s.e. 0.02) (Fig EV4 A
25 and B) suggests that active mechanisms, such as genetic interference, play a minor role in
26 REC8 positioning.

27 Secondly, the observed median distance between REC8 foci along the sister-AEs of
28 X-chromosomes was plotted against computationally generated predictions for even
29 distributed foci (indicative of active redistribution of REC8) or randomly distributed foci (Fig
30 5E) (see methods section for details). The observed median distance between REC8 foci of

1 5% of the chromosome axis length intersects the random distribution curve given the average
2 of 16 foci per chromosome (Fig 5E). We obtained the same trend when plotting the median
3 distances between foci subdivided in three categories based on the number of REC8 foci per
4 chromosome: 11-14, 15-18 and 19-22 foci. Together the two analyses indicate that the
5 seemingly uniform distribution of REC8 foci is likely due to a relative high number of foci per
6 chromosome and not a result of an active mechanism that insures an even or clustered
7 distribution.

8 The high density of REC8 foci along wild-type X-chromosomes (Fig 5) and the
9 correlation between the occurrence of LSAEs and REC8 deficiency (Fig 1 and 3) implies that
10 relative large distances between REC8 foci may lead to the occurrence of LSAEs. We tested
11 this prediction by measuring the distance between flanking REC8 foci at sites of LSAEs in
12 *Stag3* mutant spermatocytes. Indeed, we found in this mutant background, a median distance
13 of 28% of the chromosome axis length between flanking REC8 foci, significantly larger than
14 that observed for the wild-type X-chromosomes (Fig 5F).

15 In agreement with our hypothesis, illegitimate SC formation does not take place in
16 wild-type REC8-proficient zygotene spermatocytes: neither between the
17 indistinguishable/tightly associated sister-AEs of synapsing chromosomes (Fig 6A, filled
18 arrowheads) nor along yet-unsynapsed chromosomes (Fig 6B). Accordingly, we found a high
19 density of REC8 foci along the yet-unsynapsed chromosomes (average of 23 foci per
20 chromosome, Fig 6C) and a median distance between REC8 foci of 4% of the chromosome
21 axis length, which is similar to wild-type X-chromosomes yet significantly smaller than the
22 distances at LSAEs in *Stag3* mutant axes. Importantly, in contrast to REC8 foci flanking sites
23 of LSAEs we found nearly all foci in wild-type spermatocytes to be separated by distances
24 smaller than 15% of the chromosomes axis length (Fig 6E).

25 In summary, our results support a model where random positioning of a high density
26 of REC8 foci along the chromosome axes ensures that nearly all REC8 cohesin complexes
27 become separated by a distance of less than 15% of the chromosome axis length, sufficient
28 for preventing the separation of sister-AEs and illegitimate SC assembly.

29

Discussion

In this study we have analysed the individual role of the different α -kleisins for meiotic SCC and synapsis, in genetic backgrounds with different levels of cohesin function. We show that *Stag3* mutant and *Smc1b*^{-/-} spermatocytes display univalent axes interrupted by axial “openings” revealing the local appearance of two sister-AEs, referred to as local separation of AEs (LSAEs), accompanied by illegitimate SC assembly at sites of LSAEs. We also show that remaining REC8 in *Stag3* mutant spermatocytes is detected along single AEs, in most cases directly flanking sites of LSAEs, and that once the distance between REC8 foci increases to more than 15% of the chromosome axis length, LSAEs is observed. Based on these results, we propose that LSAE observed in *Stag3* mutant and *Smc1b*^{-/-}, represents local loss of REC8-mediated sister-chromatid arm cohesion.

In budding yeast, chromatin immunoprecipitation techniques (i.e. ChIP-chip and ChIP-seq) have detected cohesins predominantly enriched at the centromere and intergenic regions, and distributed in a non-random manner, approximately every 10kb along chromosome arms [37-41]. By directly quantifying and analysing the distribution of REC8 along unsynapsed sister-AEs of X-chromosomes and autosomes, as well as at sites of LSAE in *Stag3* mutant spermatocytes, we provide evidence that maintaining a high density of REC8 foci along the chromosome axes prevents the separation of sister-AEs and illegitimate SC assembly. Importantly, our analysis did not provide evidence to support the existence of an active regulatory mechanism governing the positioning of REC8 along the axes. Instead, a high density of REC8 foci, randomly distributed and separated by a minimum distance of 15% of a chromosome axis length, could be sufficient to maintain SCC. It is tempting to speculate that a dynamic, or flexible, behaviour for cohesin association with chromosomes could be in place in order to maintain SCC. In fact, in mouse and human cells, a large fraction of cohesin-binding sites on chromosomes overlap with those of the transcriptional insulator CCCTC-binding factor (CTCF) [42,43], whereas only a minor fraction of cohesin is detected with the cohesin loader subunit Scc2. Thus, cohesin could reposition from its initial binding sites on chromosomes, sliding along chromatin, while remaining topologically bound to chromosomes [44,45].

1 What is the interplay between REC8-mediated cohesion and inter-homologue SC
2 assembly? The identification of sites of LSAEs that were flanked by REC8 foci allowed us to
3 further elucidate this fundamental question. All SC components analysed (SYCP1, SYCE1,
4 SYCE2 and TEX12) were detected within the sites of LSAE along sister-AEs. Furthermore,
5 the inter-axis distances at sites of LSAEs was similar to that measured in *Rec8*-null cells,
6 indicating that inter-sister SC assembly also takes place in these sites of LSAEs.

7 Given the deleterious consequences of loss of SCC and aberrant SC assembly
8 between sister-chromatids for meiotic progression and animal fertility, meiocytes need to
9 ensure sufficient REC8 cohesin complexes along chromosome axes, possibly by controlling
10 REC8 expression, stabilization [31] and loading [46]. By comparing the levels of REC8
11 cohesin in oocytes of young versus aged mice, as well as the effect of REC8 depletion in
12 naturally aged mice, it has been proposed that increased reproductive aging correlates with
13 depletion of cohesin from chromosome arms and centromeres, leading to erroneous bi-
14 orientation in meiosis I and aneuploidy in eggs [47,48]. Thus, it could be of interest to further
15 investigate whether REC8 would be subject to an age-dependent change in
16 density/distribution along sister-AEs.

17 It has been suggested, based on the appearance of RAD21 staining of chromosomes
18 in *Rec8/Rad21L* DKO, that RAD21 could mediate canonical SCC in meiotic cells [49].
19 However, a separate study of *Rec8Rad21L* DKO mice did not detect SMC3 or RAD21
20 associated with the axial aggregates in the DKO, and also observed an increased distance
21 between sister-FISH signals, arguing that any residual cohesion in the *Rec8/Rad21L* DKO
22 would be mediated by a cohesin-independent linkage, such as DNA catenation [28].
23 Furthermore, the SC assembled between sister-AEs in *Rec8*^{-/-} spermatocytes spans 100 nm
24 [26], making it hard to envision the two sister-chromatids in this situation being entrapped by
25 RAD21-containing cohesin rings having an approximate diameter of 45 nm [50-52]. We show
26 here that RAD21 localizes along both sister-AEs at sites of LSAE, further suggesting that
27 REC8 but not RAD21-containing cohesin complexes, prevent separation of sister-AEs.

28 In addition to REC8 and RAD21, STAG3 is known to associate with RAD21L [3-5],
29 thus, a residual level of RAD21L in *Stag3* mutant mice could promote SCC. We found
30 however RAD21L foci, along both sister-AEs at sites of LSAE and illegitimate SC formation,

1 showing that RAD21L is highly unlikely to maintain canonical SCC. In agreement with this
2 result, RAD21L has been suggested to have a prominent role in DSB-independent homolog
3 association and pairing [28], not SCC.

4 In summary, our data strongly argues that REC8-containing cohesin complexes
5 provide canonical SCC, not RAD21 or RAD21L, at the prophase stage of meiosis I in
6 spermatocytes. A high density of randomly distributed REC8 cohesin complexes along the
7 axes of sister-chromatids prevents illegitimate inter-sister SC assembly, by keeping axes at a
8 distance that is too narrow to allow the assembly of the SC components.

9

Materials and methods

Mice

Stag3, *Smc1* $\beta^{-/-}$ and *Rec8* $^{-/-}$ mice have been previously described [23,25,31]. All mice were used in accordance with regulations provided by the Stockholms Norra animal ethics committee of Karolinska Institutet.

Immunostaining and antibodies

For preparation of spermatocyte spreads, a drying-down technique [53] was applied, with minor changes. In brief: single tubuli from decapsulated testes were dissected in PBS and allowed to swell in hypotonic buffer (1M Tris HCL pH 8.2; 1M Sucrose; 1M Na-citrate; 0.5M EDTA; 0.1M DTT; 0.2M PMSF; 50x EDTA-free protease-inhibitor) for 30-90mins, cells were then washed out of seminiferous tubules by thorough resuspension in 100mM sucrose solution, and fixed in 1% paraformaldehyde coated slides. Incubation of primary antibodies was done at room temperature overnight. The following primary antibodies were used: guinea pig anti-SMC1 β , and anti-C-terminal SYCP1 antibodies [54]; guinea pig anti-SYCE1, anti-SYCE2, and anti-TEX12 antibodies [14]; rabbit anti-RAD21L and anti-REC8 antibodies [4]; mouse anti-SYCP3 (sc-74569) from Santa Cruz Biotechnology; rabbit anti-RAD21 (ab154769) from Abcam; rabbit anti-SMC1 α (LS-C91803) from LifeSpan BioSciences; human anti-centromere antibody (ACA, 15-234-0001) from Antibodies Inc. The secondary antibodies used were: Alexa-488 goat anti-mouse; Alexa-555 goat anti-rabbit and goat anti-guinea pig; Alexa-647 goat anti-human (Molecular Probes Inc.). For STED microscopy secondary antibodies used were: Alexa-594 goat anti-mouse (Molecular Probes Inc.); STAR 635P goat anti-rabbit (Abberior). Prolong Gold antifade reagent without DAPI was used as mounting medium (P36930, Life Technologies). Samples were excluded if fixation or immuno-labeling were not satisfactory. Cell nuclei with compromised integrity due to preparation were also excluded. Whenever possible biological triplicates are shown.

Super-resolution fluorescence microscopy

SIM imaging was performed on a Carl Zeiss Elyra PS.1 microscope equipped with 405-, 488-, 561- and 642-nm excitation lasers. The objective used was a Plan-Apochromate 100x/1.46 oil DIC M27. Emission was collected sequentially through appropriate dichroic mirrors and bandpass filters set at 495- 575 nm for 488 nm excitation, 570-650 nm for 561 nm excitation, and above 655 nm for 642 nm excitation. SIM processing was done with the included ZEN software with selection of automatic settings for evaluation of the raw data (i.e. theoretical PSF, selection of noise filter setting, frequency weighting, baseline settings etc.) [55]. The optimal grid size was automatically assigned to each wavelength by the Zeiss Zen software, and the grid was rotated 5 times at 5 phases for each image. After evaluation, the SIM images were checked for possible artifacts (e.g. honey comb patterns of intensity in the image) so appropriate selections of evaluation settings were applied. Calibration on 40 nm beads generated a lateral precision of approximately 80 nm \pm 5nm at 488 nm excitation. Images were processed with an integrated ELYRA S system software (Zen 2011 SP2 Black).

To confirm SIM generated images super-resolution STED imaging was also applied. STED imaging was performed on a Leica SP5 TiSa STED system equipped with pulsed diode lasers (PDL 800-B, PicoQuant) for excitation at 532 nm and 640 nm and tunable near-infrared pulsed depletion laser (MaiTai, Spectra Physics). A 100X/1.4 NA chromatically red-shifted oil immersion objective lens (HCX PL APO STED, Leica Microsystems) was used for STED imaging. Fluorescence signals were passed through a 0.8-0.9 Airy unit pinhole, a dichroic mirror and separate bandpass filters (582/75 and 685/40 from Semrock) placed in front of two avalanche photodiodes. Image frames (1024x1024) were acquired sequentially line-by-line at scan speed of 600 lines per second with a pixel size of 25 nm. Images were deconvolved and processed with Huygens software (Scientific Volume Imaging).

Quantitative analysis of REC8 along chromosomes

Intensity profiles of REC8 along the X-chromosomes, asynapsed autosomes in wild-type and asynapsed chromosomes in *Stag3* mutant spermatocytes were initially measured in two

ways: a) by manually tracing the chromosome axes, labelled by SYCP3 antibody, in FIJI [56] and by an in-house constructed algorithm that automatically traced the chromosome axes and then calculated the intensity profile as maxima of seven pixel wide cross sections perpendicular to the trace. The results were found to be equally valid for peak analysis, yet the manual method handled better chromosome intersections and loops and was thus used for the data collection. All further analysis was done in MATLAB (MathWorks, Natick, MA, USA). The distances were measured as the percentage of the chromosomal axis length. The intensity data was filtered by subtracting the mean, smoothing by a 3-point moving average and finally offsetting and normalizing to the range [0,1]. A 1000-point spline interpolation was then calculated for the intensity profile and used for further analysis. The Matlab Signal Processing toolbox was used to extract the locations of all peaks of a minimum height 0.1, minimum prominence 0.04 and with a minimum peak-to-peak distance of 0.15 μm . These values were arrived at heuristically. Maxima in the raw image caused by non-chromosomal or unspecific binding were excluded based on location.

The strength of the putative REC8 foci interference was measured by fitting the frequency distribution of the inter-focus distances to the gamma distribution. The simulation of the random foci distribution was performed by random cast of 16 foci (a median number of REC8 foci, found on X-chromosome) to a chromosomal axis, repeated 100.000 times, and subsequent exclusion of the axes where inter-focus distances turned to be less than the resolution limit, i.e. 1.4% of the chromosome axis length. Importantly, the interference-related parameter ν of the simulated frequency distribution of the inter-focus distances was equal to 1.04 before the filtering, which corresponds to the random distribution [36] and corroborates the validity of the chosen method of simulation.

The generation of random and even foci distributions along the chromosomal axes was performed *in silico*. The even distribution is calculated as $d = (n-1)^{-1}$, where n denotes the number of foci and d the distance between foci. The random distribution was determined by randomly placing n foci on a chromosome. For each random placement the median distance between all foci was calculated as a fraction of the chromosome axis length and this was repeated 10,000 times for each $10 \leq n \leq 20$. The random distribution represents the average of the median of 10,000 random placements.

1

2 **Statistics**

3

4 The statistical analysis was performed with the help of GraphPad Prism 6 software
5 (GraphPad Software, Inc). *P* values reported in Figure legends are two-tailed probabilities
6 calculated by Mann–Whitney two-sided non-parametric test. The non-parametric tests were
7 used as the data distributions did not pass the D'Agostino & Pearson omnibus normality test
8 with $\alpha=0.05\%$.

9

1 **Acknowledgements**

2

3 We would like to thank S. Valentiniene for technical support, and K. Ishiguro and Y.
4 Watanabe for antibodies. We are grateful to Bennie Lemmens for invaluable comments and
5 suggestions on this manuscript. This project has received funding from the European Union's
6 (EU) Horizon 2020 research and innovation programme under grant agreement No. 634113
7 (GermAge), and has been supported by the Swedish Cancer Society, the Swedish Research
8 Council, Karolinska Institutet and Science for Life Laboratory.

9

1 **Author contributions**

2

3 AA designed, performed and analyzed the experiments/data; OM and RS did the
4 computational analysis and mathematic modeling for foci distribution; AH provided the initial
5 hypothesis; AK performed statistical analysis; HB and HB provided access and technical
6 support with super-resolution microscopy; AA and CH wrote the manuscript.

7

1 **Conflict of Interest**

2

3 The authors declare they do not have any conflict of interest.

1 **References**

2

3 1. Peters JM, Nishiyama T (2012) Sister chromatid cohesion. *Cold Spring Harbor*
4 *perspectives in biology* **4**:

5 2. Eijpe M, Offenberg H, Jessberger R, Revenkova E, Heyting C (2003) Meiotic cohesin
6 REC8 marks the axial elements of rat synaptonemal complexes before cohesins SMC1beta
7 and SMC3. *J. Cell Biol.* **160**: 657-670

8 3. Gutierrez-Caballero C, Herran Y, Sanchez-Martin M, Suja JA, Barbero JL, Llano E, Pendas
9 AM (2011) Identification and molecular characterization of the mammalian alpha-kleisin
10 RAD21L. *Cell Cycle* **10**: 1477-1487

11 4. Ishiguro K, Kim J, Fujiyama-Nakamura S, Kato S, Watanabe Y (2011) A new meiosis-
12 specific cohesin complex implicated in the cohesin code for homologous pairing. *EMBO Rep*
13 **12**: 267-275

14 5. Lee J, Hirano T (2011) RAD21L, a novel cohesin subunit implicated in linking homologous
15 chromosomes in mammalian meiosis. *J. Cell Biol.* **192**: 263-276

16 6. Lee J, Iwai T, Yokota T, Yamashita M (2003) Temporally and spatially selective loss of
17 Rec8 protein from meiotic chromosomes during mammalian meiosis. *J. Cell Sci.* **116**: 2781-
18 2790

19 7. Pezzi N, Prieto I, Kremer L, Perez Jurado LA, Valero C, Del Mazo J, Martinez AC, Barbero
20 JL (2000) STAG3, a novel gene encoding a protein involved in meiotic chromosome pairing
21 and location of STAG3-related genes flanking the Williams-Beuren syndrome deletion.
22 *FASEB J.* **14**: 581-592

- 1 8. Prieto I, Pezzi N, Buesa JM, Kremer L, Barthelemy I, Carreiro C, Roncal F, Martinez A,
2 Gomez L, Fernandez R, *et al.* (2002) STAG2 and Rad21 mammalian mitotic cohesins are
3 implicated in meiosis. *EMBO Rep* **3**: 543-550
- 4 9. Prieto I, Suja JA, Pezzi N, Kremer L, Martinez AC, Rufas JS, Barbero JL (2001)
5 Mammalian STAG3 is a cohesin specific to sister chromatid arms in meiosis I. *Nat. Cell Biol.*
6 **3**: 761-766
- 7 10. Revenkova E, Eijpe M, Heyting C, Gross B, Jessberger R (2001) Novel meiosis-specific
8 isoform of mammalian SMC1. *Mol Cell Biol* **21**: 6984-6998
- 9 11. Moses MJ (1956) Chromosomal structures in crayfish spermatocytes. *The Journal of*
10 *biophysical and biochemical cytology* **2**: 215-218
- 11 12. Westergaard M, von Wettstein D (1972) The synaptonemal complex. *Annu Rev Genet* **6**:
12 71-110
- 13 13. Costa Y, Speed R, Ollinger R, Alsheimer M, Semple CA, Gautier P, Maratou K, Novak I,
14 Hoog C, Benavente R, *et al.* (2005) Two novel proteins recruited by synaptonemal complex
15 protein 1 (SYCP1) are at the centre of meiosis. *J. Cell Sci.* **118**: 2755-2762
- 16 14. Hamer G, Gell K, Kouznetsova A, Novak I, Benavente R, Hoog C (2006) Characterization
17 of a novel meiosis-specific protein within the central element of the synaptonemal complex. *J.*
18 *Cell Sci.* **119**: 4025-4032
- 19 15. Heyting C, Dietrich AJ, Moens PB, Dettmers RJ, Offenbergh HH, Redeker EJ, Vink AC
20 (1989) Synaptonemal complex proteins. *Genome / National Research Council Canada =*
21 *Genome / Conseil national de recherches Canada* **31**: 81-87

- 1 16. Lammers JH, Offenberg HH, van Aalderen M, Vink AC, Dietrich AJ, Heyting C (1994) The
2 gene encoding a major component of the lateral elements of synaptonemal complexes of the
3 rat is related to X-linked lymphocyte-regulated genes. *Mol Cell Biol* **14**: 1137-1146
- 4 17. Meuwissen RL, Offenberg HH, Dietrich AJ, Riesewijk A, van Iersel M, Heyting C (1992) A
5 coiled-coil related protein specific for synapsed regions of meiotic prophase chromosomes.
6 *EMBO J* **11**: 5091-5100
- 7 18. Offenberg HH, Schalk JA, Meuwissen RL, van Aalderen M, Kester HA, Dietrich AJ,
8 Heyting C (1998) SCP2: a major protein component of the axial elements of synaptonemal
9 complexes of the rat. *Nucleic acids research* **26**: 2572-2579
- 10 19. Schramm S, Fraune J, Naumann R, Hernandez-Hernandez A, Hoog C, Cooke HJ,
11 Alsheimer M, Benavente R (2011) A novel mouse synaptonemal complex protein is essential
12 for loading of central element proteins, recombination, and fertility. *Plos Genet* **7**: e1002088
- 13 20. Moens PB, Pearlman RE (1988) Chromatin organization at meiosis. *Bioessays* **9**: 151-
14 153
- 15 21. Dietrich AJ, van Marle J, Heyting C, Vink AC (1992) Ultrastructural evidence for a triple
16 structure of the lateral element of the synaptonemal complex. *Journal of structural biology*
17 **109**: 196-200
- 18 22. Zickler D, Kleckner N (2015) Recombination, Pairing, and Synapsis of Homologs during
19 Meiosis. *Cold Spring Harbor perspectives in biology* **7**:
- 20 23. Revenkova E, Eijpe M, Heyting C, Hodges CA, Hunt PA, Liebe B, Scherthan H,
21 Jessberger R (2004) Cohesin SMC1 beta is required for meiotic chromosome dynamics,
22 sister chromatid cohesion and DNA recombination. *Nat. Cell Biol.* **6**: 555-562

- 1 24. Novak I, Wang H, Revenkova E, Jessberger R, Scherthan H, Hoog C (2008) Cohesin
2 Smc1beta determines meiotic chromatin axis loop organization. *J. Cell Biol.* **180**: 83-90
- 3 25. Bannister LA, Reinholdt LG, Munroe RJ, Schimenti JC (2004) Positional cloning and
4 characterization of mouse mei8, a disrupted allele of the meiotic cohesin Rec8. *Genesis* **40**:
5 184-194
- 6 26. Xu H, Beasley MD, Warren WD, van der Horst GT, McKay MJ (2005) Absence of mouse
7 REC8 cohesin promotes synapsis of sister chromatids in meiosis. *Dev. Cell* **8**: 949-961
- 8 27. Herran Y, Gutierrez-Caballero C, Sanchez-Martin M, Hernandez T, Viera A, Barbero JL,
9 de Alava E, de Rooij DG, Suja JA, Llano E, *et al.* (2011) The cohesin subunit RAD21L
10 functions in meiotic synapsis and exhibits sexual dimorphism in fertility. *EMBO J.* **30**: 3091-
11 3105
- 12 28. Ishiguro K, Kim J, Shibuya H, Hernandez-Hernandez A, Suzuki A, Fukagawa T, Shioi G,
13 Kiyonari H, Li XC, Schimenti J, *et al.* (2014) Meiosis-specific cohesin mediates homolog
14 recognition in mouse spermatocytes. *Genes Dev* **28**: 594-607
- 15 29. Parra MT, Viera A, Gomez R, Page J, Benavente R, Santos JL, Rufas JS, Suja JA (2004)
16 Involvement of the cohesin Rad21 and SCP3 in monopolar attachment of sister kinetochores
17 during mouse meiosis I. *J Cell Sci* **117**: 1221-1234
- 18 30. Xu H, Beasley M, Verschoor S, Inselman A, Handel MA, McKay MJ (2004) A new role for
19 the mitotic RAD21/SCC1 cohesin in meiotic chromosome cohesion and segregation in the
20 mouse. *EMBO Rep* **5**: 378-384
- 21 31. Fukuda T, Fukuda N, Agostinho A, Hernandez-Hernandez A, Kouznetsova A, Hoog C
22 (2014) STAG3-mediated stabilization of REC8 cohesin complexes promotes chromosome
23 synapsis during meiosis. *EMBO J* **33**: 1243-1255

- 1 32. Hopkins J, Hwang G, Jacob J, Sapp N, Bedigian R, Oka K, Overbeek P, Murray S, Jordan
2 PW (2014) Meiosis-specific cohesin component, Stag3 is essential for maintaining
3 centromere chromatid cohesion, and required for DNA repair and synapsis between
4 homologous chromosomes. *Plos Genet* **10**: e1004413
- 5 33. Winters T, McNicoll F, Jessberger R (2014) Meiotic cohesin STAG3 is required for
6 chromosome axis formation and sister chromatid cohesion. *EMBO J* **33**: 1256-1270
- 7 34. Solari AJ (1969) Changes in the sex chromosomes during meiotic prophase in mouse
8 spermatocytes. *Genetics* **61**: Suppl:113-120
- 9 35. Solari AJ (1970) The spatial relationship of the X and Y chromosomes during meiotic
10 prophase in mouse spermatocytes. *Chromosoma* **29**: 217-236
- 11 36. de Boer E, Stam P, Dietrich AJ, Pastink A, Heyting C (2006) Two levels of interference in
12 mouse meiotic recombination. *Proc Natl Acad Sci U S A* **103**: 9607-9612
- 13 37. Blat Y, Kleckner N (1999) Cohesins bind to preferential sites along yeast chromosome III,
14 with differential regulation along arms versus the centric region. *Cell* **98**: 249-259
- 15 38. Glynn EF, Megee PC, Yu HG, Mistrot C, Unal E, Koshland DE, DeRisi JL, Gerton JL
16 (2004) Genome-wide mapping of the cohesin complex in the yeast *Saccharomyces*
17 *cerevisiae*. *PLoS Biol* **2**: E259
- 18 39. Lengronne A, Katou Y, Mori S, Yokobayashi S, Kelly GP, Itoh T, Watanabe Y, Shirahige K,
19 Uhlmann F (2004) Cohesin relocation from sites of chromosomal loading to places of
20 convergent transcription. *Nature* **430**: 573-578
- 21 40. Megee PC, Mistrot C, Guacci V, Koshland D (1999) The centromeric sister chromatid
22 cohesion site directs Mcd1p binding to adjacent sequences. *Mol Cell* **4**: 445-450

- 1 41. Tanaka T, Cosma MP, Wirth K, Nasmyth K (1999) Identification of cohesin association
2 sites at centromeres and along chromosome arms. *Cell* **98**: 847-858
- 3 42. Parelho V, Hadjur S, Spivakov M, Leleu M, Sauer S, Gregson HC, Jarmuz A, Canzonetta
4 C, Webster Z, Nesterova T, *et al.* (2008) Cohesins functionally associate with CTCF on
5 mammalian chromosome arms. *Cell* **132**: 422-433
- 6 43. Wendt KS, Yoshida K, Itoh T, Bando M, Koch B, Schirghuber E, Tsutsumi S, Nagae G,
7 Ishihara K, Mishiro T, *et al.* (2008) Cohesin mediates transcriptional insulation by CCCTC-
8 binding factor. *Nature* **451**: 796-801
- 9 44. Haering CH, Farcas AM, Arumugam P, Metson J, Nasmyth K (2008) The cohesin ring
10 concatenates sister DNA molecules. *Nature* **454**: 297-301
- 11 45. Ocampo-Hafalla MT, Uhlmann F (2011) Cohesin loading and sliding. *J Cell Sci* **124**: 685-
12 691
- 13 46. Visnes T, Giordano F, Kuznetsova A, Suja JA, Lander AD, Calof AL, Strom L (2014)
14 Localisation of the SMC loading complex Nipbl/Mau2 during mammalian meiotic prophase I.
15 *Chromosoma* **123**: 239-252
- 16 47. Chiang T, Schultz RM, Lampson MA (2011) Age-dependent susceptibility of chromosome
17 cohesion to premature separase activation in mouse oocytes. *Biol Reprod* **85**: 1279-1283
- 18 48. Lister LM, Kouznetsova A, Hyslop LA, Kalleas D, Pace SL, Barel JC, Nathan A, Floros V,
19 Adelfalk C, Watanabe Y, *et al.* (2010) Age-related meiotic segregation errors in mammalian
20 oocytes are preceded by depletion of cohesin and Sgo2. *Curr Biol* **20**: 1511-1521

- 1 49. Llano E, Herran Y, Garcia-Tunon I, Gutierrez-Caballero C, de Alava E, Barbero JL,
2 Schimenti J, de Rooij DG, Sanchez-Martin M, Pendas AM (2012) Meiotic cohesin complexes
3 are essential for the formation of the axial element in mice. *J Cell Biol* **197**: 877-885
- 4 50. Gruber S, Haering CH, Nasmyth K (2003) Chromosomal cohesin forms a ring. *Cell* **112**:
5 765-777
- 6 51. Haering CH, Lowe J, Hochwagen A, Nasmyth K (2002) Molecular architecture of SMC
7 proteins and the yeast cohesin complex. *Mol Cell* **9**: 773-788
- 8 52. Haering CH, Schoffnegger D, Nishino T, Helmhart W, Nasmyth K, Lowe J (2004)
9 Structure and stability of cohesin's Smc1-kleisin interaction. *Mol Cell* **15**: 951-964
- 10 53. Peters AH, Plug AW, van Vugt MJ, de Boer P (1997) A drying-down technique for the
11 spreading of mammalian meiocytes from the male and female germline. *Chromosome Res.* **5**:
12 66-68
- 13 54. Kouznetsova A, Novak I, Jessberger R, Hoog C (2005) SYCP2 and SYCP3 are required
14 for cohesin core integrity at diplotene but not for centromere cohesion at the first meiotic
15 division. *J. Cell Sci.* **118**: 2271-2278
- 16 55. Komis G, Mistrik M, Samajova O, Ovecka M, Bartek J, Samaj J (2015) Superresolution
17 live imaging of plant cells using structured illumination microscopy. *Nature protocols* **10**:
18 1248-1263
- 19 56. Schindelin J, Arganda-Carreras I, Frise E, Kaynig V, Longair M, Pietzsch T, Preibisch S,
20 Rueden C, Saalfeld S, Schmid B, *et al.* (2012) Fiji: an open-source platform for biological-
21 image analysis. *Nature methods* **9**: 676-682
- 22
23

Figure Legends

Figure 1. Visualization of sister-chromatid axes and sites of local separation of axial elements with super-resolution microscopy.

A) Representative nuclear spreads of wild-type pachytene and *Rec8*^{-/-} pachytene-like spermatocytes. Nuclear spreads were immunostained for SYCP3 and ACA. Magnified views are indicated by dashed areas. Schematic representation on magnified chromosomes represents tightly associated sister-AEs (separated for easier representation) in paired wild-type homologs, and the appearance of two distinguishable/separated sister-AEs once REC8-mediated cohesion is lost in *Rec8*^{-/-} univalents. Bars, 10 µm in spreads and 1 µm on insets.

B) Representative nuclear spread of zygotene-like *Stag3* mutant spermatocytes. Nuclear spreads were immunostained for SYCP3 and ACA. Magnified views are indicated by dashed areas. Schematic representation on magnified univalents represents: separation of sister-AEs (centre) and close association of sister-AEs (right). Bellow: graph showing the percentages of axes with: separation of AEs (dark grey area) and closely associated AEs (light grey area). 414 axes analysed, from 11 nuclei. Bars, 10 µm in spreads and 1 µm on insets.

C) Magnified views of zygotene-like *Stag3* mutant univalents with LSAEs. Nuclear spreads were immunostained for SYCP3 and ACA. Schematic representation indicates sites of LSAEs. Bellow: graph showing the percentages of axes with: LSAEs (red area), extensive separation of AEs (dark grey area) and closely associated AEs (light grey area). 414 axes analysed, from 11 nuclei. Bars, 1 µm.

D) Representative nuclear spread of zygotene-like *Smc1β*^{-/-} spermatocytes. Nuclear spreads were immunostained for SYCP3 and ACA. Magnified views are indicated by dashed areas. Schematic representation on magnified univalents represents sites of LSAEs. Bellow: graph showing the percentages of axes with: LSAEs (red area), extensive separation of AEs (dark

grey area) and closely associated AEs (light grey area). 404 axes analysed, from 10 nuclei.
Bars, 10 μ m in spreads and 1 μ m on insets.

E) STED images of representative zygotene-like *Stag3* mutant and *Smc1 β ^{-/-}* univalents displaying LSAEs. Nuclear spreads were immunostained for SYCP3. Bars, 1 μ m.

F) Graph indicating the inter-axis distances measured in wild-type pachytene bivalents; pachytene-like *Rec8^{-/-}* and zygotene-like *Stag3* mutant and *Smc1 β ^{-/-}* univalents. Each measurement in wild-type and *Rec8^{-/-}* corresponds to the median of 3 distances measured along one homolog (n=60). Each measurement in *Stag3* mutant and *Smc1 β ^{-/-}* mutant axes correspond to 1 distance measured at sites of local separation of AEs (n=40 and n=20, respectively). Horizontal lines indicate median.

G) Graph indicating the inter-axis distances measured at terminally and centrally located sites of LSAEs in zygotene-like *Stag3* mutant univalents. Each measurement corresponds to 1 distance measured at terminally (n=20) and centrally (n=20) located sites of local separation of axial elements. Horizontal lines indicate median.

H) Schematic representation of the axis architecture observed in the different backgrounds analysed: close association of sister-AEs rendering a single AE per homolog (wild-type), separation of sister-AEs, with appearance of two individual sister-AEs (*Rec8^{-/-}*), and LSAEs rendering local “axial openings” with two individual sister-AEs (*Stag3* mutant and *Smc1 β ^{-/-}*). Centromeres are shown in red. For easier comparison of distance between axes, a red bar of equal length was added to each chromosome drawing.

Figure 2. Inter-sister SC formation takes place within sites of local separation of axial elements.

A) Representative wild-type pachytene bivalents; pachytene-like *Rec8^{-/-}*, zygotene-like *Stag3* mutant and *Smc1 β ^{-/-}* univalents. Nuclear spreads were immunostained for SYCP1, SYCP3

1 and ACA. Filled arrowheads indicate sites of LSAEs with detectable SYCP1. Bars, 1 μ m.
2 Bellow: graphs showing the percentages of sites of LSAEs with detectable SC assembly
3 along sister-AEs of *Stag3* mutant and *Smc1 β ^{-/-}* univalents (n=120 and n=68, respectively).

5 B) Representative zygotene-like *Stag3* mutant univalents. Nuclear spreads were
6 immunostained for SYCP3, ACA and: SYCE1, SYCE2 and TEX12. Filled arrowheads indicate
7 SC assembly between sites of LSAEs. Bars, 1 μ m

9 C) Quantification of signal distribution within sites of LSAEs, in *Stag3* mutant spermatocytes.
10 Signal distribution measured for SYCP3 and: SYCP1, SYCE1, SYCE2 and TEX12. Empty
11 arrowheads indicate signal intensity peaks that correspond to each of the two sister-chromatid
12 axes, filled arrowheads indicate SYCP1 peaks.

14 **Figure 3. Localization of α -kleisins REC8, RAD21L and RAD21 in relation to sites with**
15 **local separation of axial elements.**

17 A) Representative zygotene-like *Stag3* mutant and *Smc1 β ^{-/-}* univalents. Nuclear spreads
18 were immunostained for SYCP3, SYCE1 and REC8. Bellow: graph showing the percentages
19 of *Stag3* mutant axes with sites of LSAEs with and without flanking REC8 foci. 78 axes with
20 LSAEs were analysed. Bars, 1 μ m.

22 B) Representative pachytene-like *Rec8^{-/-}*, zygotene-like *Stag3* mutant and *Smc1 β ^{-/-}*
23 univalents. Nuclear spreads were immunostained for SYCP3, SYCE1 and RAD21L. Bars, 1
24 μ m.

26 C) Representative zygotene-like *Stag3* mutant and *Smc1 β ^{-/-}* univalents. Nuclear spreads
27 were immunostained for SYCP3, SYCE1 and RAD21. Bars, 1 μ m.

29 D) Schematic representation of univalents axes (black lines) with sites of LSAEs, and relative
30 distribution of REC8 (green), RAD21L grey) and RAD21 (grey).

Figure 4. Narrow inter-axis distance prevents illegitimate SC formation along sister-chromatids of wild-type X-chromosomes.

A) Representative wild-type pachytene sex chromosomes. Nuclear spreads of pachytene spermatocytes were immunostained for SYCP3. Filled arrowheads indicate the PAR. Dashed area indicated in centre panel corresponds to the magnified view on the right panel. Bars, 10 μ m in spreads and 1 μ m on insets.

B) Graph indicating the inter-axis distances measured at sites of local separation of axial elements in zygotene-like *Stag3* mutant univalents and along pachytene wild-type X-chromosomes. Each measurement in the X-chromosomes corresponds to the median of 3 distances (according to the scheme in figure) (n=54). Each measurement in *Stag3* mutant corresponds to 1 distance measured at sites with local separation of axial elements (n=40). Horizontal lines indicate median. $p < 0.0001$, obtained with two-tailed Mann-Whitney test. Below: schematic representation of the XY pair: sister-AEs are coloured in black and grey for easier visualization. Filled arrowhead indicates PAR. Purple bars in scheme indicate regions where inter-axis distances are measured.

C) Representative pachytene wild-type sex chromosomes. Nuclear spreads of pachytene spermatocytes were immunostained for SYCP3 and SYCE2. Dashed area indicated in centre panel corresponds to the magnified view on the right panel. Empty arrowhead indicates two discernable sister-AEs without SYCE2. Bars, 10 μ m in spreads and 1 μ m on insets.

Figure 5. Analysis of REC8 distribution along the sister-chromatid axes of wild-type X-chromosomes.

A) Analysis of REC8 distribution in representative pachytene wild-type sex chromosomes. Nuclear spreads of pachytene spermatocytes were immunostained for SYCP3 and REC8. Bars, 10 μ m in spreads and 1 μ m on insets. Magnified XY pair is indicated by dashed area.

1 Scatterplot showing the number of REC8 foci per X-chromosome. 225 foci identified in 14 X-
2 chromosomes. Horizontal line indicates the mean, error bars indicate s.d. 3.02.
3
4 B) Top: representative computationally straightened pachytene wild-type X-chromosomes.
5 Nuclear spreads were immunostained for SYCP3 and REC8. Chromosomes were aligned at
6 the PAR, and subdivided into 25 regular intervals. Bar, 1 μ m. Bellow: histogram showing the
7 distribution of the percentages of REC8 foci (n=225) among 25 regular intervals along 14 X-
8 chromosomes. Dotted line indicates mean.
9
10 C) Histogram showing the relative frequency of inter-REC8 distances along X-chromosomes.
11 211 inter-REC8 distances from 14 X-chromosomes. Grey area represents 15% of the
12 chromosome axis length. The respective cumulative distribution function is shown.
13
14 D) Histogram showing the best fit of the observed inter-REC8 distances to the gamma
15 distribution. Green curve indicates the best fit of the observed inter-REC8 distances. v
16 indicates the value for which the best fit was obtained, with estimated standard error 0.27.
17
18 E) Graph comparing the median distance of REC8 foci with computationally predicted even
19 and random distributions. Median distances between foci subdivided in three categories (11-
20 14, 15-18 and 19-22 REC8 foci per chromosome). Purple asterisk indicates the median
21 distance of all REC8 foci.
22
23 F) Scatterplot comparing inter-REC8 distances along on X-chromosomes with the distances
24 between flanking REC8 foci at sites of LSAEs in the *Stag3* mutant. 211 inter-REC8 distances
25 measured along X-chromosomes and 10 distances measured between flanking REC8 foci in
26 *Stag3* mutant. Grey area represents 15% of the chromosome axis length. Horizontal lines
27 indicate the median. $p < 0.0001$, obtained with two-tailed Mann-Whitney test.
28
29 **Figure 6. Analysis of REC8 distribution along the sister-chromatid axes of wild-type**
30 **autosomes.**

1

2 A) Representative yet-unsynapsed autosome from wild-type zygotene spermatocytes.
3 Nuclear spreads were immunostained for SYCP3 and SYCE2. Magnified autosome is
4 indicated by dashed area. Filled arrowheads indicate yet-unsynapsed axes regions. Bars, 10
5 μm in spreads and 1 μm on insets

6

7 B) Representative unsynapsed autosome from wild-type zygotene spermatocytes. Nuclear
8 spreads were immunostained for SYCP3, REC8 and ACA. Magnified autosome is indicated
9 by dashed area. Bars, 10 μm in spreads and 1 μm on insets.

10

11 C) Scatterplot comparing the average number of REC8 foci along zygotene autosomes and
12 X-chromosomes. Number of REC8 foci were quantified along 15 zygotene autosomes and 14
13 X-chromosomes. Each dot represents the number of REC8 foci on each chromosome. Total
14 number of foci identified: zygotene autosomes (343), X-chromosomes (225). Horizontal lines
15 indicate the mean, error bars indicate s.d.: 7.42 and 3.02 for zygotene autosomes and X-
16 chromosomes, respectively. $p = 0.0060$, obtained with two-tailed Mann-Whitney test.

17

18 D) Histogram showing the relative frequency of inter-REC8 distances along yet-unsynapsed
19 zygotene autosomes. 294 inter-REC8 distances analyzed in 14 chromosomes. Grey area
20 represents 15% of the chromosome axis length. The respective cumulative distribution
21 function is shown.

22

23 E) Scatterplot comparing the measured inter-REC8 distances on yet-unsynapsed zygotene
24 autosomes, X-chromosomes and sites of LSAEs in *Stag3* mutant. Number of inter-REC8
25 distances for yet-unsynapsed zygotene autosomes, X-chromosomes and sites of local
26 separation of axial elements in *Stag3* mutant, $n=294$, $n=211$ and $n=10$, respectively.
27 Horizontal lines indicate the median. $p < 0.0001$, obtained with two-tailed Mann-Whitney test.

Expanded View Figure Legends

Figure EV1. Chromosomal localization of SC components in wild-type and mutant spermatocytes with reduced cohesin function.

A) Representative whole nuclei of wild-type pachytene; pachytene-like *Rec8*^{-/-} and zygotene-like *Stag3* mutant and *Smc1β*^{-/-} spermatocytes. Nuclear spreads were immunostained for SYCP1, SYCP3 and ACA. Filled arrowheads indicate the bivalent and univalents shown on Fig 2A. Bars, 10 μm.

B) Representative whole nuclei of zygotene-like *Stag3* mutant spermatocytes. Nuclear spreads were immunostained for SYCP3, ACA and each of the following SC components: SYCE1, SYCE2 and TEX12. Filled arrowheads indicate the univalents shown on Fig 2B. Bars, 10 μm.

Figure EV2. Chromosomal localization of meiotic α-kleisins during prophase I.

A) Representative nuclear spreads of wild-type spermatocytes. Nuclear spreads from leptotene to diplotene stages of meiotic prophase were immunostained for REC8 and SYCP3. Bars, 10 μm.

B) Representative nuclear spreads of wild-type spermatocytes. Nuclear spreads from leptotene to diplotene stages of meiotic prophase were immunostained for RAD21 and SYCP3. Bars, 10 μm.

C) Representative nuclear spreads of wild-type spermatocytes. Nuclear spreads from leptotene to diplotene stages of meiotic prophase were immunostained for RAD21 and SYCP3. Bars, 10 μm.

Figure EV3. Chromosomal localization of α-kleisins in relation to sites of local

1 separation of axial elements and SC formation, in mutant spermatocytes with reduced
2 cohesin function.

3
4 A) Representative whole nuclei of zygotene-like *Stag3* mutant and *Smc1 β ^{-/-}* spermatocytes.
5 Nuclear spreads were immunostained for REC8, SYCE1 and SYCP3. Filled arrowheads
6 indicate the *Stag3* mutant and *Smc1 β ^{-/-}* univalents shown on Fig 3A. Bars, 10 μ m.

7
8 B) Representative whole nuclei of zygotene-like *Stag3* mutant and *Smc1 β ^{-/-}* spermatocytes.
9 Nuclear spreads were immunostained for RAD21L, SYCE1 and SYCP3. Filled arrowheads
10 indicate the *Stag3* mutant and *Smc1 β ^{-/-}* univalents shown on Fig 3B. Bars, 10 μ m.

11
12 C) Representative whole nuclei of zygotene-like *Stag3* mutant and *Smc1 β ^{-/-}* spermatocytes.
13 Nuclear spreads were immunostained for RAD21, SYCE1 and SYCP3. Filled arrowheads
14 indicate the *Stag3* mutant and *Smc1 β ^{-/-}* univalents shown on Fig 3C. Bars, 10 μ m.

15
16 D) Representative whole nuclei from early zygotene-like to pachytene-like stages in *Rec8^{-/-}*
17 spermatocytes. Nuclear spreads were immunostained for RAD21L, SYCE1 and SYCP3.
18 Magnified views on E are represented by dashed areas on nuclear spreads. Filled arrowhead
19 indicates the *Rec8^{-/-}* univalent shown on Fig 3B. Bars, 10 μ m.

20
21 E) Magnified views of *Rec8^{-/-}* univalents shown in D. Magnified univalents from early
22 zygotene-like to pachytene-like stages of meiotic prophase were immunostained for RAD21L,
23 SYCE1 and SYCP3. Bars, and 1 μ m.

24
25 **Figure EV4. Gamma probability distribution modeling of inter-focus distances.**

26
27 A) Histogram showing the relative frequency of computationally generated inter-focus
28 distances (grey bars) and the best fit of the distances to the gamma distribution (blue curve).
29 v' indicates the value for which the best fit was obtained. Estimated standard error 0.02.

1 B) Graph comparing the best fit of the observed inter-REC8 distances to the gamma
2 distribution (green curve), and the best fit of computationally generated inter-focus distances
3 (dashed curve). v indicates the value for which the best fit was obtained for the inter-REC8
4 distances, with estimated standard error 0.27. v' indicates the value for which the best fit was
5 obtained for the computationally generated inter-focus distances, with estimated standard
6 error 0.02.

Figure 1. Agostinho et al.

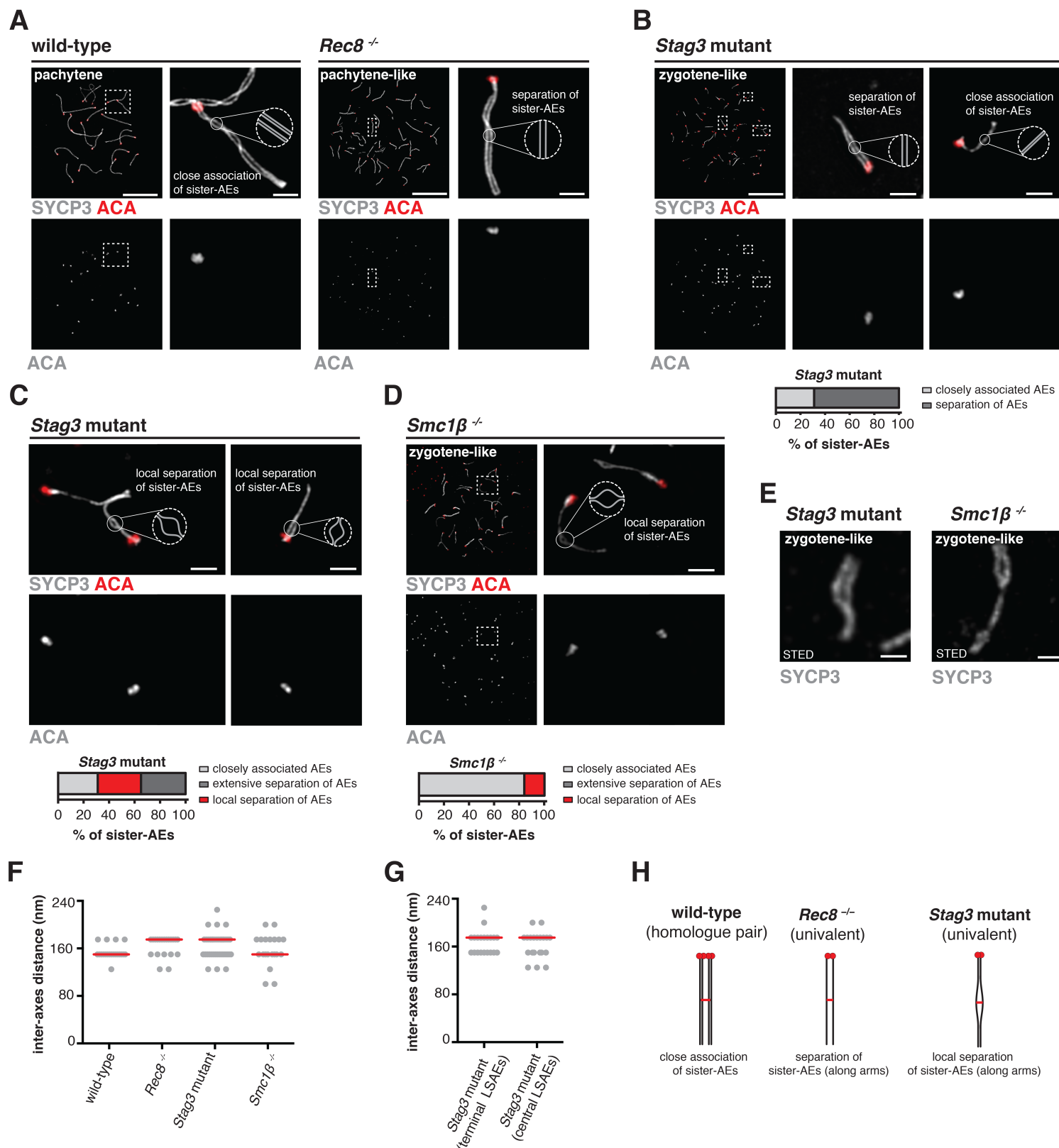


Figure 2. Agostinho et al.

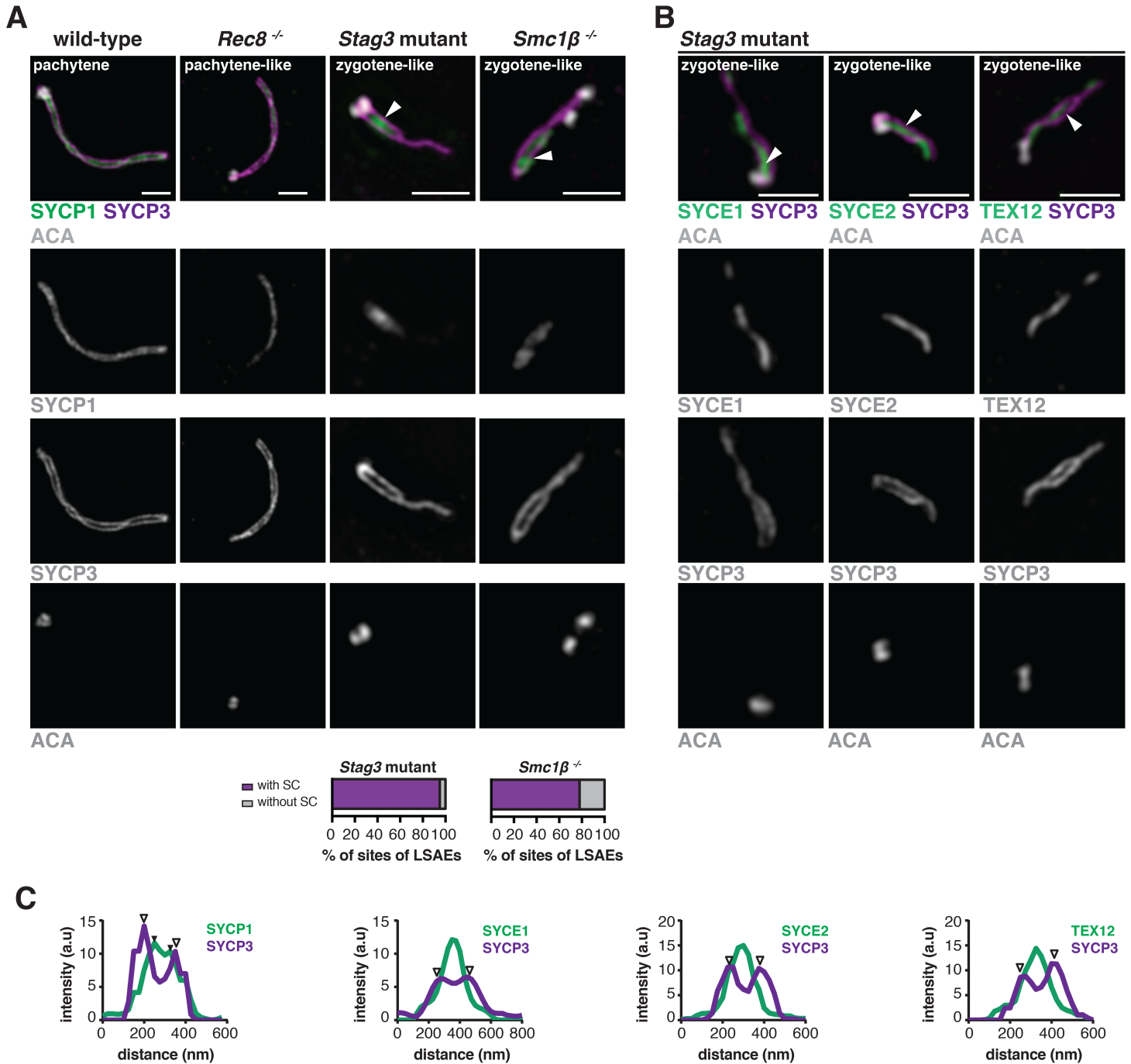


Figure 3. Agostinho et al.

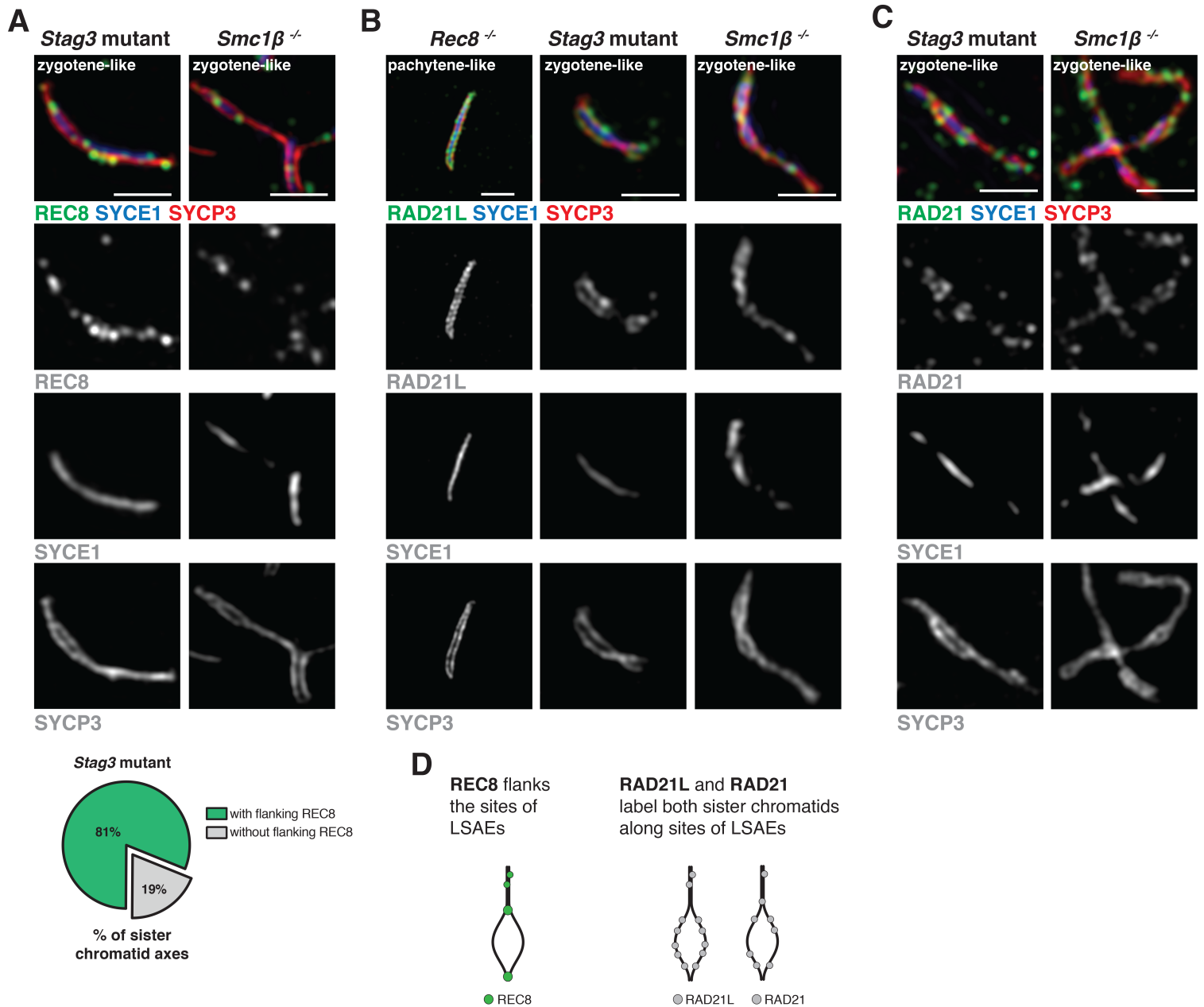
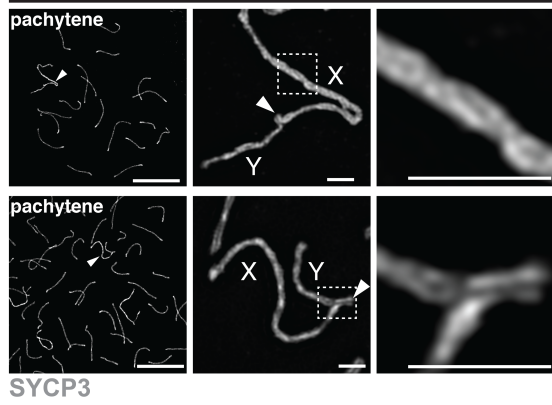


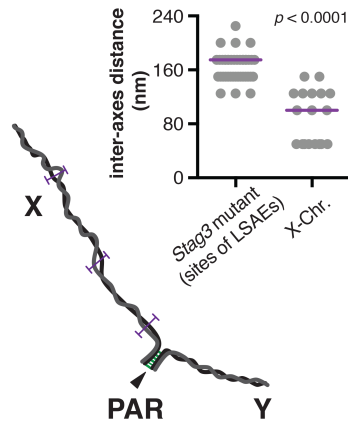
Figure 4. Agostinho et al.

A

wild-type



B



C

wild-type

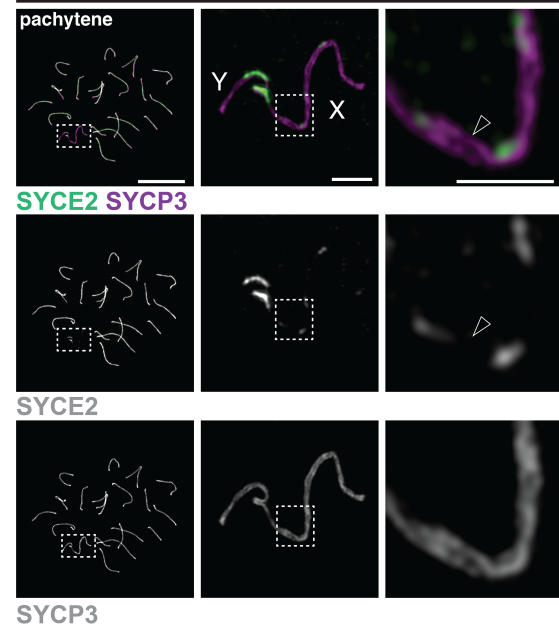


Figure 5. Agostinho et al.

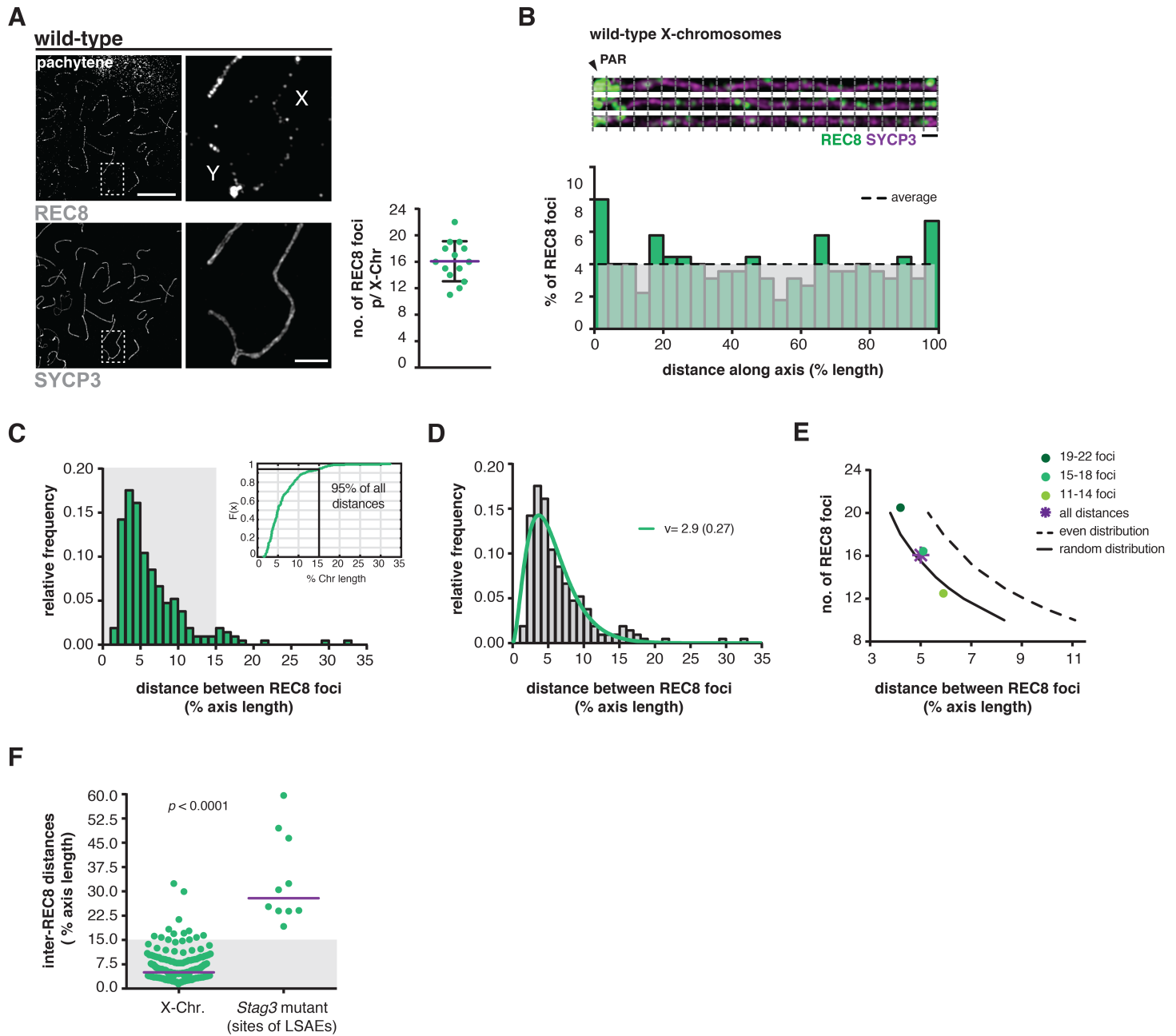


Figure 6. Agostinho et al.

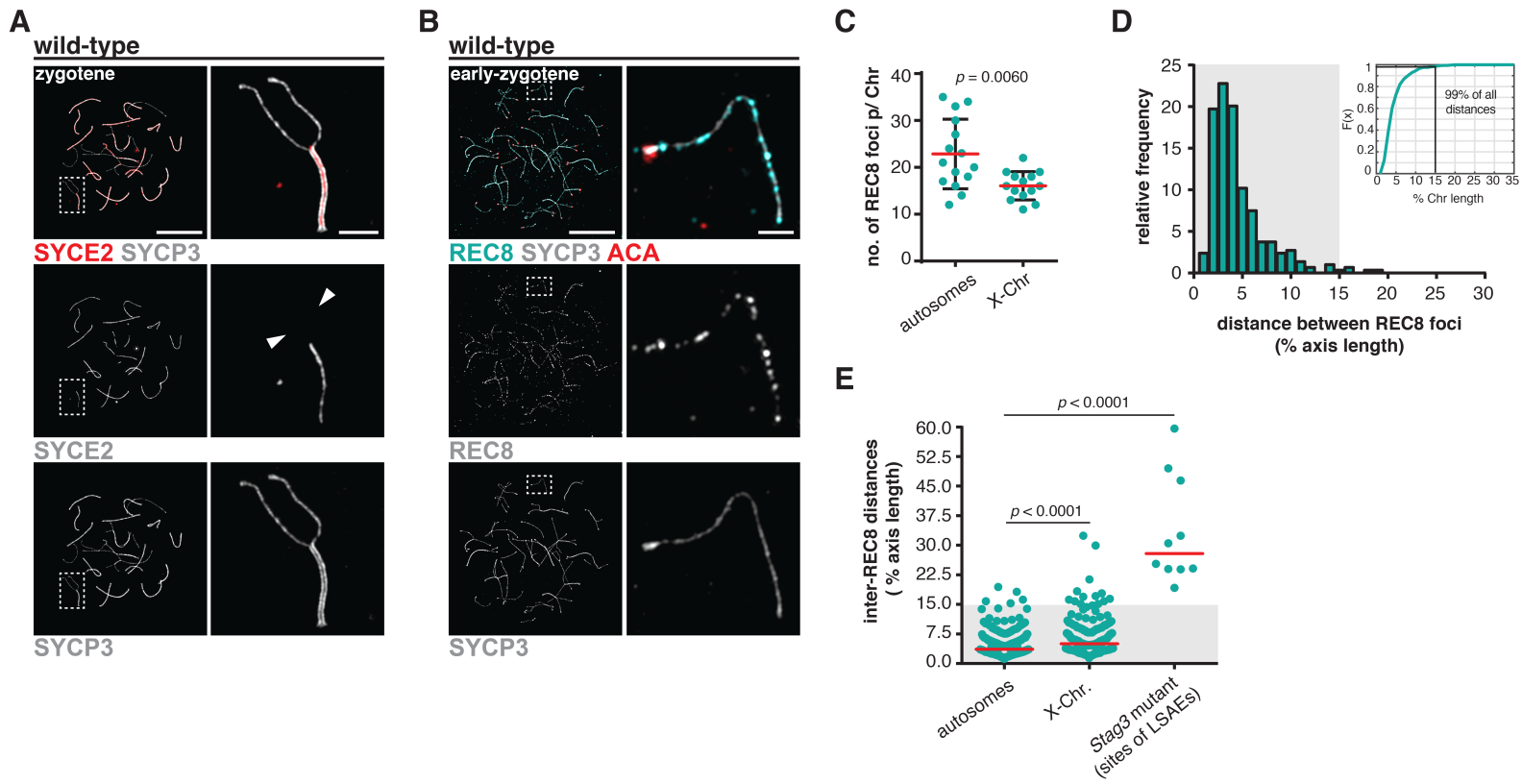
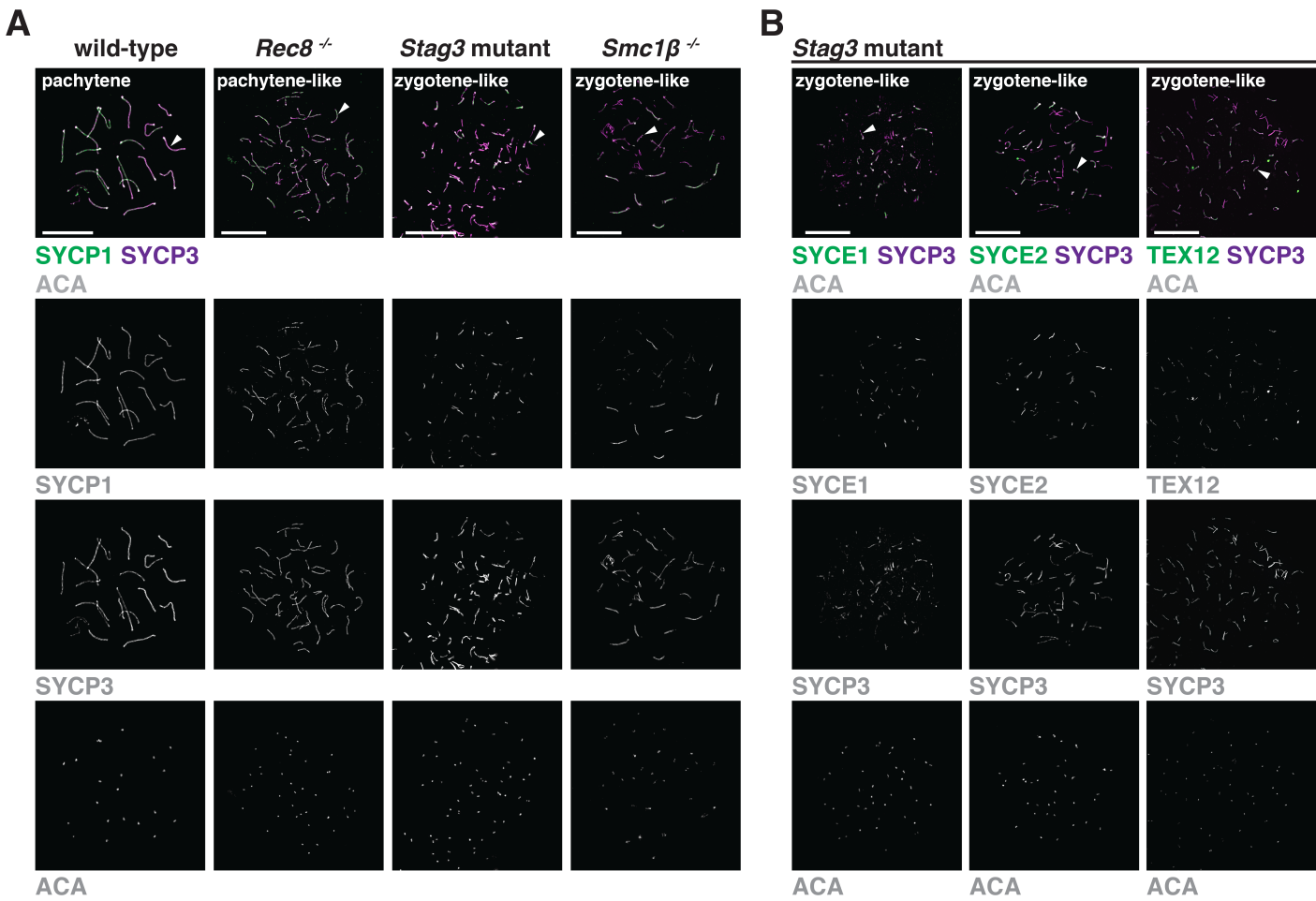
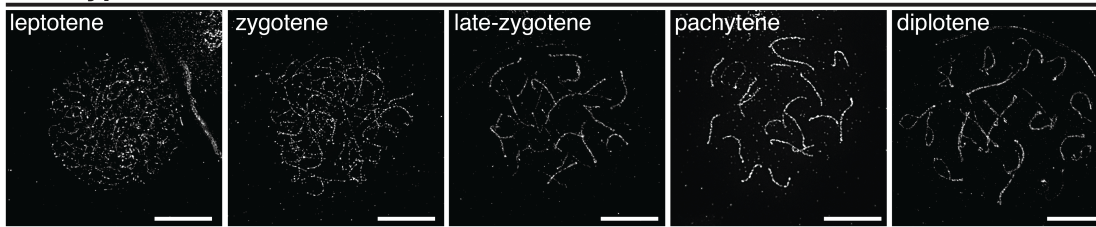


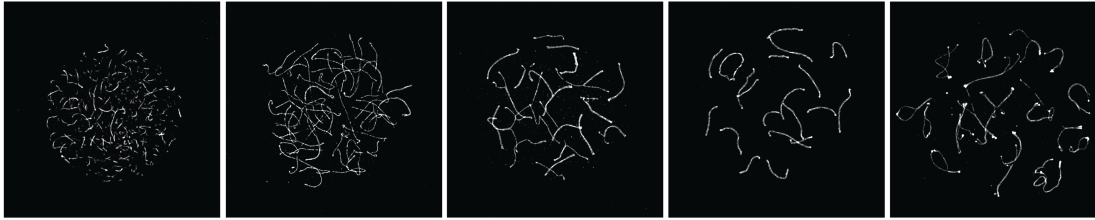
Figure EV1 . Agostinho et al.



A
wild-type

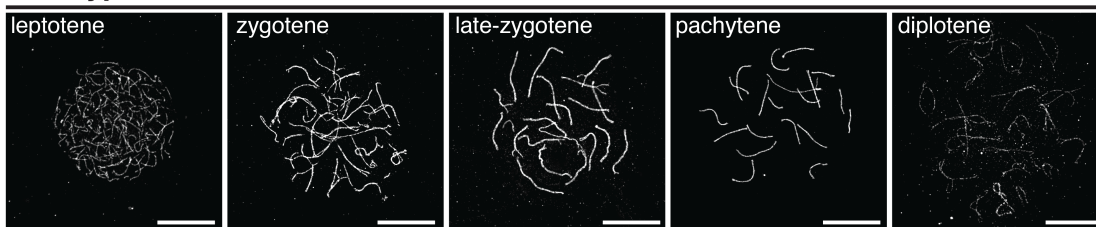


REC8



SYCP3

B
wild-type

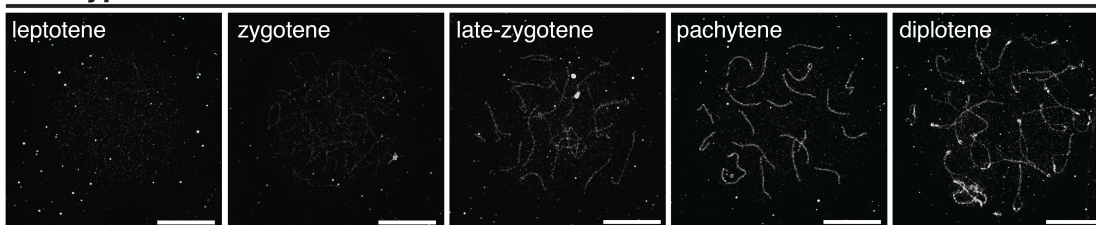


RAD21L



SYCP3

C
wild-type



RAD21



SYCP3

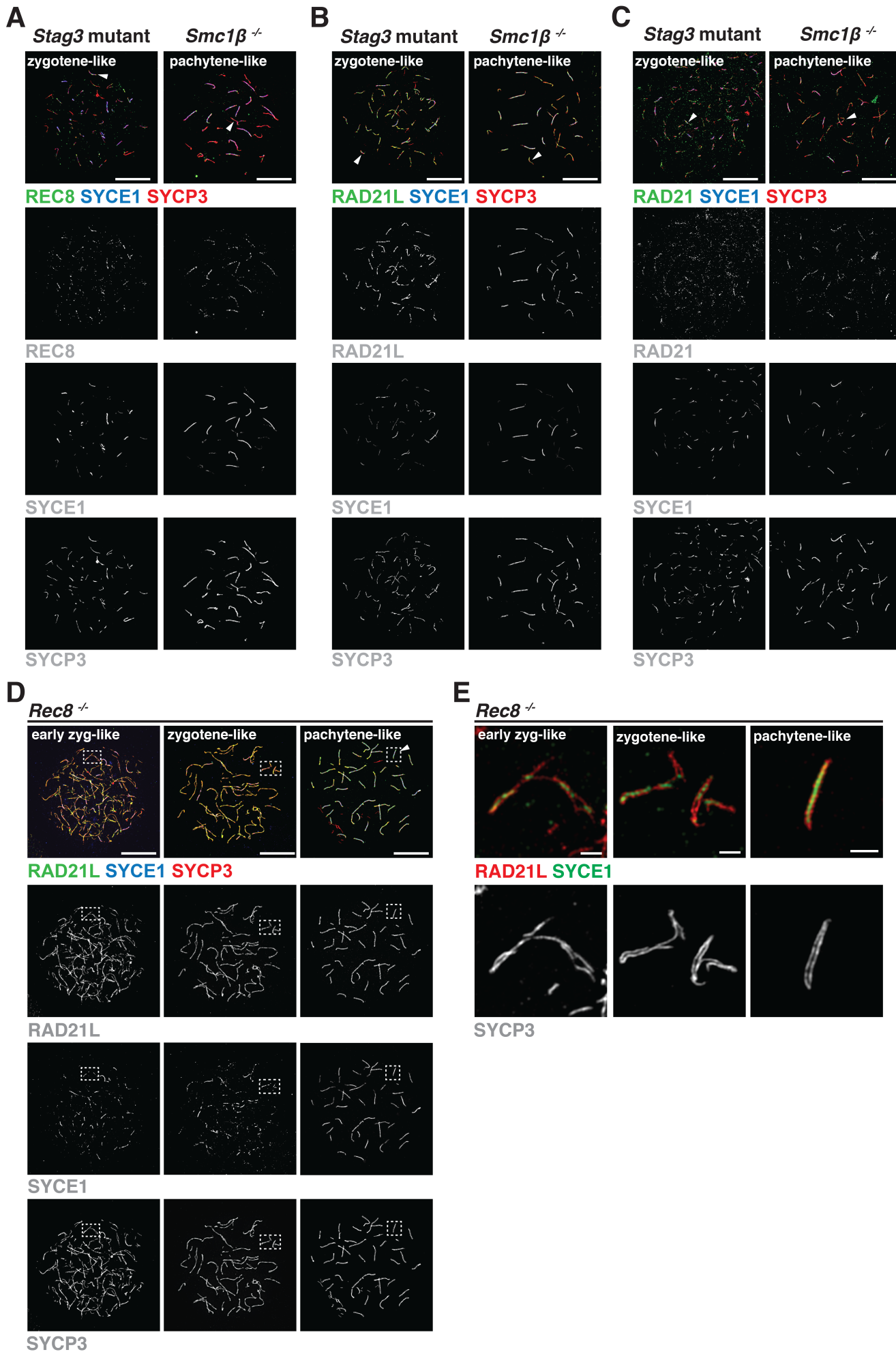


Fig EV4. Agostinho et al.

